



RESEARCH ARTICLE

10.1029/2017JC013741

Key Points:

- Energetic high-frequency (period < 2 hr) oscillations induced by atmospheric disturbances can drive large velocities in freshwater estuaries
- Meteorologically induced water level oscillation flow, in comparison with river-dominated flow, plays an important role in sediment transport
- Asymmetry of bottom shear stress induced by meteorologically induced water level oscillations can alter patterns of sediment transport

Correspondence to:

C. H. Wu,
chinwu@engr.wisc.edu

Citation:

Linares, Á., Wu, C. H., Anderson, E. J., & Chu, P. Y. (2018). Role of meteorologically induced water level oscillations on bottom shear stress in freshwater estuaries in the Great Lakes. *Journal of Geophysical Research: Oceans*, 123, 4970–4987. <https://doi.org/10.1029/2017JC013741>

Received 28 DEC 2017

Accepted 19 JUN 2018

Accepted article online 27 JUN 2018

Published online 23 JUL 2018

Role of Meteorologically Induced Water Level Oscillations on Bottom Shear Stress in Freshwater Estuaries in the Great Lakes

Álvaro Linares¹ , Chin H. Wu¹ , Eric J. Anderson² , and Philip Y. Chu²

¹Department of Civil and Environmental Engineering, University of Wisconsin-Madison, Madison, WI, USA, ²Great Lakes Environmental Research Laboratory, National Oceanic and Atmospheric Administration, Ann Arbor, MI, USA

Abstract The role of meteorologically induced water level oscillations (MIWLOs) on bottom shear stresses in a freshwater estuary in the Great Lakes is investigated. Atmospheric data including air pressure, wind speed and direction, and radar reflectivity are compiled, and comprehensive field measurements including velocity profiles, water levels, river discharges, and bottom sediment properties in the Manistique River (MR) estuary, Michigan, are conducted. Wavelet and cross-wavelet analysis reveals that large velocity events (>0.5 m/s) in the MR estuary are generated by high-frequency MIWLOs (i.e., meteotsunamis and high-frequency seiches) induced by energetic oscillations in air pressure and/or wind speed and direction with periods below 2 hr. Measured velocity profiles reveal that MIWLO-dominated conditions can increase bottom shear stress by an order of magnitude in comparison with river-dominated flow conditions. The hydrodynamic model indicates that bottom shear stresses under both the downstream and upstream flows during the MIWLO-dominated event were significantly larger than those during river-dominated conditions. The interactions of MIWLOs and flood flows can significantly alter the bottom shear stresses in the main river channel, and MIWLOs are revealed to be the principal resuspension mechanism in areas such as the upstream tributary branches where flood flows individually do not cause resuspension. Furthermore, the role of MIWLOs asymmetry in fresh water Great Lakes estuaries on velocity residuals and net sediment transport is revealed and discussed. Overall, this paper fills important knowledge gaps in the role of MIWLOs on sediment transport in enclosed basin estuaries, thus providing essential information for coastal management and estuarine remediation.

1. Introduction

Bottom shear stress induced by hydrodynamic flows plays an important role in contaminated sediment transport, critical to remediation efforts in the river or estuaries of Areas of Concern (AOC) in the US and Canada (International Joint Commission, 1978, 1989). In the Great Lakes estuaries, where mixing of salt and tidal flow is negligible (Trebitz, 2006), river flows, horizontal temperature gradients, and meteorologically induced water level oscillations (MIWLOs) are the main physical mechanisms affecting hydrodynamic conditions (Bedford, 1992; Green & Coco, 2014; Linares et al., 2016; Quinn, 1988; Sorensen et al., 2004). In particular, velocities induced by MIWLOs in estuaries can be or exceed an order of magnitude higher than those induced by horizontal temperature gradients (Hlevca et al., 2015) or by river flows (Pattiaratchi & Wijeratne, 2015). As a result, flow reversals in estuaries with large discharges are commonly observed (Derecki & Quinn, 1990; McLaren & Singer, 2008; Sorensen et al., 2004). Amplitudes of MIWLOs in the Great Lakes can reach from a few centimeters to 2–3 m (As-Salek & Schwab, 2004; Bechle & Wu, 2014; Schwab, 1978). With periods ranging from a few minutes to several hours (Bedford, 1992; Defant, 1961), the long wave characteristics of MIWLOs can exert shear stresses above thresholds to resuspend bottom sediments in the river and estuary environments. Moreover, MIWLOs, one of the major flushing mechanisms in riverine estuaries or shallow coastal embayments (Hlevca et al., 2015; Rueda & Cowen, 2005; Wells & Sealock, 2009), can affect the residence time of contaminated sediments and in turn remediation decisions of AOC in the Great Lakes. In view of the consequences of MIWLOs, it is important to better understand the role of MIWLOs on bottom shear stress and sediment transport in rivers and estuaries.

Seiches, one type of MIWLOs, are basin-scale standing waves frequently observed in an enclosed or semi-enclosed water body (As-Salek & Schwab, 2004; Bedford, 1992) and periods of waves are determined by

©2018. The Authors.

This is an open access article under the terms of the Creative Commons Attribution-NonCommercial-NoDerivs License, which permits use and distribution in any medium, provided the original work is properly cited, the use is non-commercial and no modifications or adaptations are made.

the size and geometry of the basin (Rabinovich, 2009). Seiches can be generated by the cessation of atmospheric wind forcings (Gardner et al., 2006; Rao et al., 1976) or the sudden shifting of wind directions (Derecki & Quinn, 1990; Rabinovich, 2009). In the past, some efforts have been paid to investigate the effects of seiches on sediment transport in Great Lakes estuaries. For instance, McLaren and Singer (2008) found that the oscillatory nature of seiches, instead of flood flows, was more likely to transport sediments in the Buffalo River. This type of high-amplitude river seiches connected to the Great Lakes can induce flow reversals (Bedford, 1992; Singer et al., 2008; Trebitz, 2006) in the Detroit River (Derecki & Quinn, 1990; Quinn, 1988), the St. Louis River (Sorensen et al., 2004), or the Buffalo River (McLaren & Singer, 2008). The features of reversal flows can even transport contaminated sediments (Schneider et al., 2002) to previously cleaned up areas in the upstream of rivers, thus degrading the expected outcomes of remediation efforts. Overall, previous studies have illustrated the importance of seiches and called for further insights on the effects of seiches on sediment transport in Great Lakes estuaries.

Meteotsunamis are MIWLOs with periods ranging from a few minutes to 2 hr (Rabinovich, 2009; Rabinovich & Monserrat, 1996). Different from seiches, meteotsunamis are subbasin-scale propagating waves generated by subsynoptic-scale fast-moving atmospheric disturbances in barometric pressure or wind (Anderson et al., 2015; Bechle & Wu, 2014; Monserrat et al., 2006; Šepić et al., 2016). Heights of meteotsunamis can be amplified if the propagation speed of atmospheric perturbations is approximately equal to that of the meteotsunami wave, that is, $c = \sqrt{gd}$ with g as the gravitational constant and d as the water depth for open oceanic or lake water waves (Proudman, 1929) or $c = gT \tan [\beta(2n + 1)]/2\pi$ with β as the shelf slope and T as the wave period for coastal edge waves (Greenspan, 1956). Meteotsunamis occur more often than expected. Recent studies show that meteotsunamis with wave height larger than 0.3 m occur more than 100 times per year in the Great Lakes (Bechle et al., 2016). For example, Linares et al. (2016) identified 11 meteotsunamis with amplitudes between 0.15 and 0.74 m occurring in the Manistique River (MR) in Lake Michigan during a 2-month period in the summer of 2012. With amplitudes on the order of a few centimeters, meteotsunamis can induce strong currents in coastal embayments (Vilibić et al., 2004, 2008), likely resuspending and transporting bottom sediments in river and coastal estuaries. While occurrences and causes of meteotsunamis have been recently investigated, the role of meteotsunamis on bottom shear stress and sediment transport in estuarine environments remains unclear.

Interactions between MIWLOs and river flows can significantly alter benthic boundary layer structures (Bedford & Abdelrhman, 1987; Green, 1992; Wang, 2002), thus affecting transport of bottom sediments. In natural river flows, boundary layers are typically turbulent (Werner et al., 2003) with a nearly constant stress close to the bottom where the mean velocity profile can be approximated by a logarithmic shape (Wright, 1989). In contrast, boundary layer structures in oceanic estuarine environments can be substantially affected by the interaction between tides and natural river flows (Cai et al., 2014; Heathershaw & Langhorne, 1988; Hoitink & Jay, 2016; Kuo et al., 1996). The magnitudes of bottom shear stress are thereby affected due to the nonlinearity of the friction term in the momentum balance equation (Godin, 1999). For example, Lueck and Lu (1996) observed that bottom stresses fluctuated up to an order of magnitude during the interaction of tides and river flows, in comparison with those during tidal wave propagation (Cai et al., 2014; Godin, 1999). In Great Lakes estuaries where the tidal influence on velocities is negligible, MIWLOs have an analogous role to tides, but the periods are much shorter (Bedford, 1992). Furthermore, MIWLOs, unlike tides, do not exhibit regular oscillatory patterns due to a wide range of periods for transient waves. To date, numerous studies have investigated the interactions between tides and river flows in ocean estuaries. Nevertheless, bottom shear stresses due to interactions between MIWLOs and river flows in fresh water estuaries or coastal systems with weak tidal effects have yet to be reported, as far as the authors are aware.

The purpose of this paper is to examine the role of MIWLOs and their interactions with river flows on bottom shear stress in the MR, Michigan, as an example of a nontidal or Great Lakes estuary. First, we identify the causes of large velocity fluctuations in the MR based on field measurements. Velocity profiles and bottom shear stresses under MIWLO-dominated and flow-dominated conditions are investigated and compared. At last, the spatial patterns of maximum bottom shear stresses induced by MIWLOs are examined and revealed using a 3D hydrodynamic model. In the following, section 2 describes the study site. Section 3 details the field measurements, data analysis, and hydrodynamic modeling. Results are presented in section 4. In section 5, the validity of bottom shear stress estimates is assessed. Furthermore, bottom shear stresses caused by interactions of MIWLOs and flood flows in the MR are discussed. Asymmetry of velocity and bottom shear stress due to MIWLOs is investigated and revealed. Summary and conclusions are given at the last.

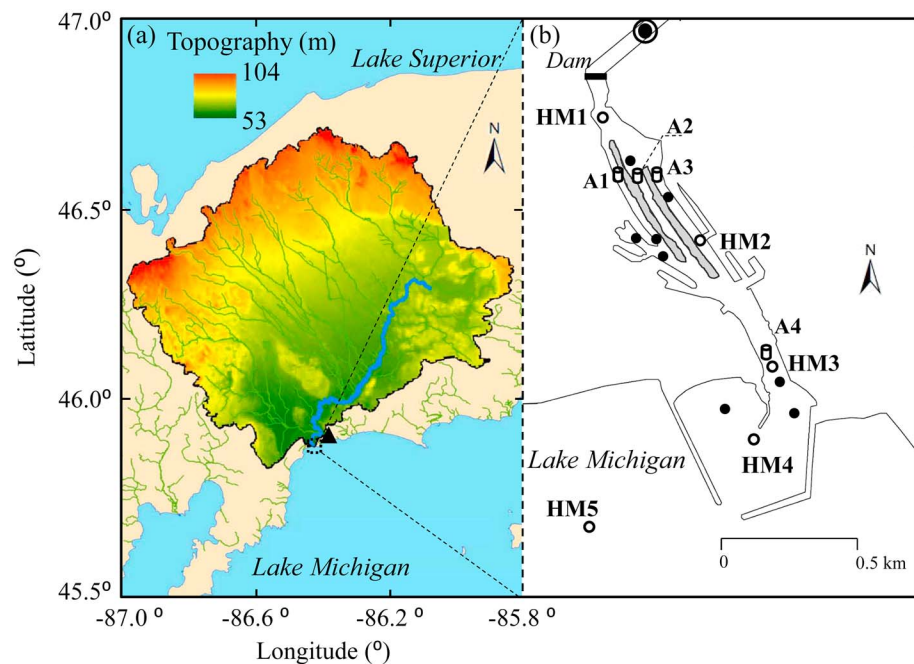


Figure 1. (a) The Manistigue River (MR) watershed basin consisting of a National Oceanic and Atmospheric Administration Automated Surface Observing System weather station at Manistique Schoolcraft airport (filled triangle) and the MR study site (dotted square); and (b) locations of field measurements at the MR: sediment cores (filled circles), five HOBOS sensor for water level observations (open circles), four acoustic Doppler current profilers for three-dimensional velocity observations (cylinders), and one United States Geological Survey flow gage (surrounded solid circle).

2. Study Site

The MR, located in the Upper Peninsula of Michigan, is a 114-km-length river within a 3,742-km² watershed flowing into Lake Michigan (Figure 1a). The downstream 2.7 km of the MR and harbor has been listed as one of the Great Lakes AOC due to sediment contamination with polychlorinated biphenyls and historical waste from sawmills and a paper mill. The MR includes an upstream non-operated dam and a downstream protected harbor connected to Lake Michigan (Figure 1b). Three narrow (~40-m-wide) upstream channels and four river branches in the middle of the MR converge into a downstream main channel that connects the upper MR with the harbor area. The bathymetry of MR is generally shallow (Figure 2a). The average water depth is 2 m, and the navigation channel is maintained to have a depth of 4 m extending from the harbor mouth (Figure 2b). The shallow water depth tends to hinder the influence of horizontal temperature gradients, and the breakwater protection reduces wind waves inside the MR estuary, yielding MIWLOs and river flows to be the main forcing mechanisms affecting bottom shear stress. Overall, the study site is a shallow estuary exposed to MIWLOs and river flow forcings, similar to many other AOCs of the Great Lakes (McLaren & Singer, 2008; Trebitz et al., 2002).

3. Methods

3.1. Data and Field Measurements

Air pressure, wind speed, and wind direction data with a sampling period of 1 min are obtained from a National Weather Service Automated Surface Observing System station located at Manistique Schoolcraft airport (KISQ), as shown in Figure 1a. Mosaic radar reflectivity images obtained from the National Oceanic and Atmospheric Administration National Climatic Data Center are employed to identify storms with potential to generate meteotsunamis following the methodology in Bechle et al. (2015). River flow data from 1938 to 2016 are obtained from a flow gage at the MR (United States Geological Survey, 04056500), as shown in Figure 1b. Offshore wind wave heights and directions are obtained from the northern Lake Michigan buoy 45002 (45°20'39"N 86°24'41"W) of the National Oceanic and Atmospheric Administration National Data Buoy Center, http://www.ndbc.noaa.gov/station_page.php?station=45002.

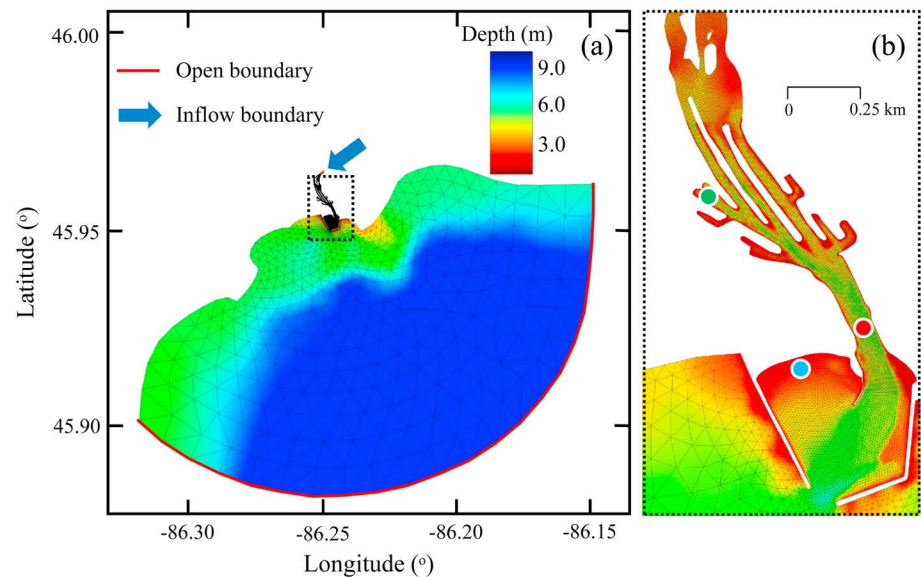


Figure 2. (a) Unstructured meshes on the bathymetry of the Manistique River (MR) and the extended open boundaries. (b) Zoom in on the MR detailing the high-grid spatial resolution.

Comprehensive field measurements including nearshore bathymetry, bottom sediment properties, water levels, and velocity profiles in the MR were conducted during June–August 2012 and 15–28 August 2016. Specifically, the nearshore bathymetry and substrates were mapped using a Tritech SeaKing subbottom profiler and a Towfish side scan sonar with a submeter Trimble GPS (Lin et al., 2010). Sediment cores (undisturbed Shelby tube soil samples with 7.3-cm inner diameter, ASTM D-1587-08, 2007) at eight sites covering the spatial variability of the MR (Figure 1b) were collected to characterize critical shear stress depth profiles. Water levels along the MR were measured using five HOBO pressure sensors (U20-001-01; range: 0 to 9 m; accuracy: ± 0.5 cm) with a sampling frequency of 1 min. Four HOBO sensors, denoted as HM1 to HM4, were distributed from the upstream to the harbor mouth along the longitudinal direction of the MR (Figure 1b). One HOBO sensor, designated as HM5, was located offshore in Lake Michigan. Water depth measured by HOBOs is converted into water level oscillations by subtracting the mean depth of the recording period from 15 to 28 August 2016 as a reference datum in this paper. Three dimensional velocity profile measurements with a 2-min ensemble interval were obtained with three Nortek acoustic Doppler current profilers (ADCPs; range: ± 10 m/s; accuracy ± 0.5 cm/s), located in each of the three upstream narrow channels, denoted as A1–A3, during 27 June and 29 August 2012. In 2016, one ADCP was deployed in the main channel (A4) for 14 days. Near-bottom three-dimensional velocity measurements with a 16-Hz sampling frequency were collected with a Nortek acoustic Doppler velocimeter (range: ± 4 m/s; accuracy ± 0.1 cm/s) in the same location as ADCP A4 during 27 June and 29 August 2012.

3.2. MIWLO Identification

Velocity, water level, wind wave, and atmospheric pressure, and wind data are processed to identify meteorologically induced water level oscillations with periods less than 2 hr. In Lake Michigan, the periods of low-frequency water level fluctuations for the natural oscillation modes of the basin are between 2.20 and 9 hr (Defant, 1961). Thus, in this study, a high-pass filter (period ≤ 2 hr) is used to extract the high-frequency components of MIWLOs at the MR and the high-frequency component of barometric pressure at KISQ. Note that high-frequency MIWLOs are composed of two types: meteotsunamis and high-frequency seiches. Meteotsunamis are identified under the three following criteria: (i) period of water level oscillations is between 2 min and 2 hr; (ii) wave height exceeds 5 cm; and (iii) an associated storm structure is detected with radar reflectivity images (Bechle et al., 2015). High-frequency seiches are identified if criteria (i) and (ii) are met but not (iii).

3.3. Contribution of Pressure and Wind Stress Calculation

Relative contribution of pressure and wind stress to meteotsunami generation is assessed using the method detailed in Linares et al. (2016) and is briefly described here. Pressure and wind contributions are obtained by

the integrals over the barometric pressure and wind stress atmospheric disturbances, respectively, denoted as $P^* = \frac{1}{\rho_w g} \Delta P$ and $W^* = \frac{1}{\rho_w g} \sum \frac{\tau_i}{H} U \Delta t_{wi}$, where ρ_w is the density of water, g is the acceleration constant, ΔP is the variation in barometric pressure within the pressure disturbance, H is the water depth, and τ_i is the shear stress during the time duration of the wind disturbance. The temporal resolution of time interval, Δt_{wi} , is 1 min. Relative contribution for pressure and wind stress can thereby be calculated as $\%P = P^*/(P^* + W^*)$ and $\%W = W^*/(P^* + W^*)$, respectively.

3.4. Wavelet Analysis

Wavelet spectral analysis (Daubechies, 1990; Torrence & Compo, 1998) has been applied to air pressure (Tanaka, 2010), wind speed (Linares et al., 2016), and water level (Candella, 2009; Hlevca et al., 2015; Linares et al., 2016) to analyze the relationship between the time-frequency content of causative atmospheric perturbations and the resultant water levels in meteotsunamis. Specifically, Linares et al. (2016) employed the wavelet power spectrum (WPS) analysis of atmospheric disturbances and water level fluctuations to quantitatively reveal the role of wind speed and air pressure on meteotsunamis in northern Lake Michigan. Furthermore, cross-wavelet spectral analysis (Grinsted et al., 2004) with the cross-wavelet power spectra (CWPS) was employed to quantitatively depict the joint variability in the time-frequency content of two signals (e.g., air pressure or wind speed) with water level fluctuations. In this study, we use the WPS and CWPS analysis (Linares et al., 2016) to depict the relations between atmospheric forcing (e.g., wind and air pressure) and MIWLOs at water levels inside (HM3) and outside (HM5) of the harbor and velocity measurements at site A4.

3.5. Bottom Shear Stress Estimate and Critical Shear Stress Measurement

Bottom shear stress (τ_b) induced by MIWLOs is estimated using $\tau_b = \rho_w u_*^2$, where u_* is the shear or friction velocity obtained by fitting velocity observations to a logarithmic profile (LP) within a fully turbulent boundary layer under uniform flow conditions (Biron et al., 2004; Kim et al., 2000; Wilcock, 1996; Wright, 1989). In this study, velocity observations from the lower portion of the water column at site A4 are used. Specifically, the velocity bins used for bottom shear stress calculations are located between 0.20 and 1.25 m above the bottom, with a spacing of 0.20 m. We fit the velocity profile by starting from the lowest three velocity bins and continuously adding one more bin until the regression coefficient of determination $R^2 \geq 0.995$ (Kim et al., 2000; Lueck & Lu, 1996; Wilcock, 1996). Once the bottom shear stress is larger than the critical shear stress, denoted τ_c , sediment resuspension occurs (Dey, 1999; Partheniades, 2009; Shields, 1936). Vertical profiles of critical shear stress for the sediment cores ranging from 15- to ~45-cm length collected in the MR are experimentally obtained using the Automated Sediment Erosion Testing System, developed by Lee et al. (2004). The surface critical shear stress varies from 0.07 to 0.13 Pa with a mean value of $\tau_c = 0.1$ Pa and a standard deviation of 0.04 Pa, consistent with critical shear stress studies in sandy sediments (e.g., Lin & Wu, 2013, 2014; Miller et al., 1977; Shvidchenko et al., 2001). The critical shear stresses below the surface range from 0.2 to 4 Pa, similar to the values reported in other studies (Lee et al., 2004; Partheniades, 2009). Additionally, bottom sediment particle sizes are obtained by conducting sieve analysis following the ASTM standards (ASTM D-2487-98, 2000). Results of particle size distributions and the survey using the Towfish side scan sonar indicate that bottom in the MR is predominantly formed with (<5% passing the #200 sieve) fine sand sediments ($D_{50} = 0.2$ mm).

3.6. Hydrodynamic Modeling

The Semi-Implicit Cross-Scale Hydrosience Integrated System Model based upon the 3D shallow-water equations with hydrostatic and Boussinesq approximations is used to simulate MIWLOs at the MR. The Semi-Implicit Cross-Scale Hydrosience Integrated System Model, developed by Zhang and Baptista (2008) and Zhang et al. (2016), has been applied to study sediment transport (Pinto et al., 2012), storm surge response (Bertin et al., 2011), inundation (Cho et al., 2012), tsunamis (Zhang et al., 2011), and meteotsunamis (Bechle & Wu, 2014; Linares et al., 2016). Previously, Linares et al. (2016) employed the Semi-Implicit Cross-Scale Hydrosience Integrated System Model to the whole Lake Michigan and the MR by a total of 213,500 unstructured triangular elements with sizes ranging from 5 m inside the MR to 1 km in the midlake. In this study, we further increase the horizontal resolution ranging from 2 m inside the MR to 250 m in Lake Michigan, yielding 265,170 triangular elements (Figure 2). The vertical depth is further divided from 10 Sigma layers in Linares et al. (2016) into 30 Sigma layers, leading to a vertical resolution varying from 2 to

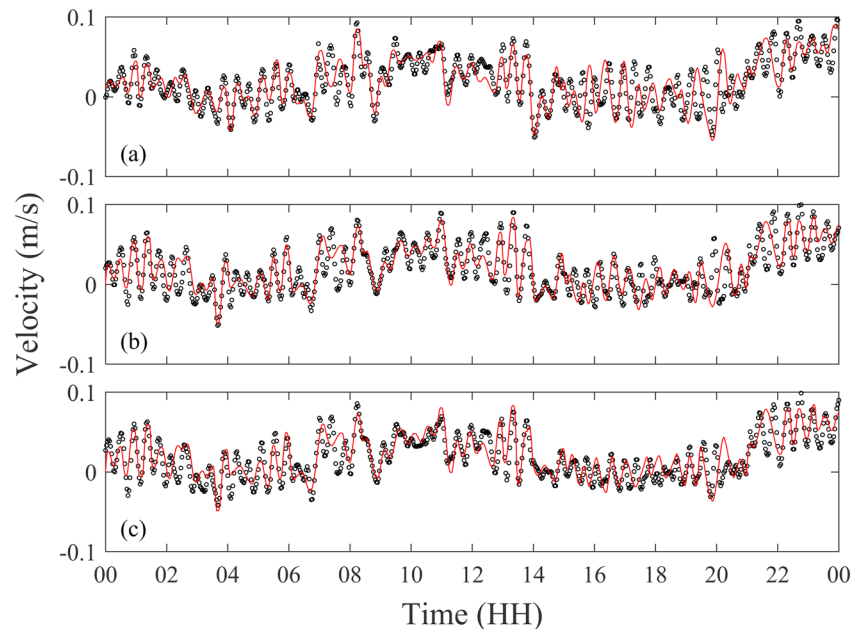


Figure 3. Observed (black) and modeled (red) depth-averaged current velocity during 26 June 2012 at (a) A3-East channel, (b) A2-middle channel, and (c) A-1 west channel.

9 cm at near bottom cells within the MR. A LP formula with a quadratic drag coefficient dependent on the bed roughness length z_0 (Pinto et al., 2012) is used to calculate bottom shear stress using the last bottom computational cell. The time step employed is $\Delta t = 10$ s, satisfying the stability requirements for the semi-implicit scheme.

Model calibration is conducted by comparing model results against observed water level oscillations at outside (HM5) and inside (HM1–4) the MR from the period of 26 June 2012. For the inflow boundary condition, observed hourly upstream river discharge by the United States Geological Survey gage, ranging between 20.7 and 21.6 m^3/s , is used (Figure 2a). Observed MIWLOs are used as a downstream open boundary condition that represents Lake Michigan water level oscillations (Figure 2a). To avoid spurious reflection of waves in the domain, open boundary conditions are optimized based upon the adjoint method (Sasaki et al., 1955; Shulman et al., 1998) by iterating the water level input at the open boundary until the deviation between observed and modeled water levels at HM5 is minimized. The adjoint method is widely used in oceanography studies to optimize open boundary forcings in hydrodynamic simulations of estuaries subjected to tidal (e.g., Blayo & Debreu, 2005; Seiler, 1993; Wang et al., 2014) and subtidal forcings (Liu & Gan, 2016). In this study, the control variables, that is, the variables with respect to which the optimization is run, are the amplitudes and phases of the main oscillation modes of the water level observed at HM5. Bed roughness length z_0 with a range of 0.0025–0.0035 m is calibrated throughout the domain to minimize deviations between observed and modeled velocities in the three upstream channels. Figure 3 shows that the model captures the high variability of depth-averaged velocity directions (reversed flow) and magnitudes with a root mean square error (RMSE) of 0.0206, 0.0178, and 0.0169 m/s in the western (A1), mid (A2), and eastern (A3) channels, respectively. Similar to the previous calibration results (see Figure 4 in Linares et al., 2016), the model with the finer resolution with the open boundary forcing has excellent agreement with water level observations inside and outside the MR (not shown here for brevity), with the RMSE of 0.0261, 0.0121, 0.0128, 0.0134, and 0.0130 m at HM1–HM5, respectively.

Model validation is performed for the period of 29 August 2012 with observed MIWLOs and flow velocity in the upstream narrow channels in the MR. Figure 4 shows that during this period, Lake Michigan water levels oscillated with maximum amplitude of 0.03 m, which was amplified to 0.07-m oscillations inside the MR. The channel flow discharge ranged between 11.7 and 13.1 m^3/s . RMSE values for water level comparison are 0.0160, 0.0191, 0.0122, 0.0182, and 0.0121 m at HM1–HM5, respectively. The RMSE values of flow velocity are 0.0171, 0.0153, and 0.0159 m/s in the western (A1), mid (A2), and eastern (A3) channels, respectively.

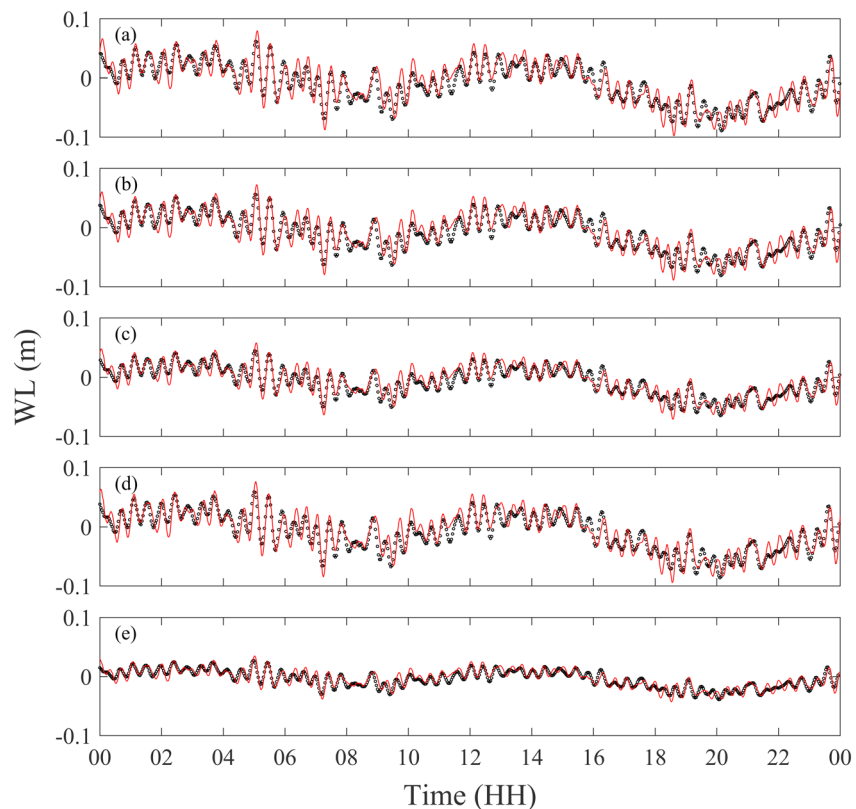


Figure 4. Observed (black) and modeled (red) water level (WL) oscillations during 29 August 2012 at (a) HM1, (b) HM2, (c) HM3, (d) HM4, and (e) HM5.

Overall, the excellent validation with RMSE less than 0.002 m in water level and 0.02 m/s in velocity indicates that the model configuration and calibration is suitable to simulate hydrodynamic conditions in the MR induced by river flow and Lake Michigan MIWLOs. To the best of the authors' knowledge, this is the first time that an open boundary using MIWLOs forcing is employed to simulate hydrodynamics in freshwater estuaries in the Great Lakes.

4. Results

4.1. MIWLO Events

Eight meteotsunami events associated with large velocity fluctuations during the study period of August 2016 are identified (Figure 5). These eight events are denoted at the top of Figure 5 by letter C that stands for convective storm and by letters P, W, or PW if the event is characterized as pressure driven ($P^* > 60\%$), wind driven ($W^* > 60\%$), or pressure and wind driven ($40\% < P^* < 60\%$ and $40\% < W^* < 60\%$), respectively. The time series of wind speed and barometric pressure exhibit abrupt changes associated with the meteotsunamis (Figures 5e and 5f, respectively). Based upon the classification, four meteotsunamis were pressure-driven, two were wind-driven, and two were driven by both pressure and wind. The ratio of meteotsunami-causative forcing is consistent with the observed meteotsunamis in the summer of 2012 in the MR (Linares et al., 2016), confirming that either air pressure, wind, or both can generate meteotsunamis in Lake Michigan. In contrast, four seiche events (denoted from S1 to S4 at the bottom of Figure 5) with large flow velocities (Figure 5a) were observed inside (Figure 5b) and outside (Figure 5c) of the MR during the study period. Air pressure did not exhibit significant fluctuations during the four high-frequency seiche events, suggesting that wind disturbance is the key to initiate seiches. Specifically, the S1 event simultaneously occurred with wind speed that decreased from 7 to 5 m/s and maintained a constant wind direction afterward. The S2 event was associated with wind speed that increased from 2 to 4 m/s with a direction change up to 20° . Both S3 and S4 events were associated with increasing and rapidly fluctuating wind speeds but

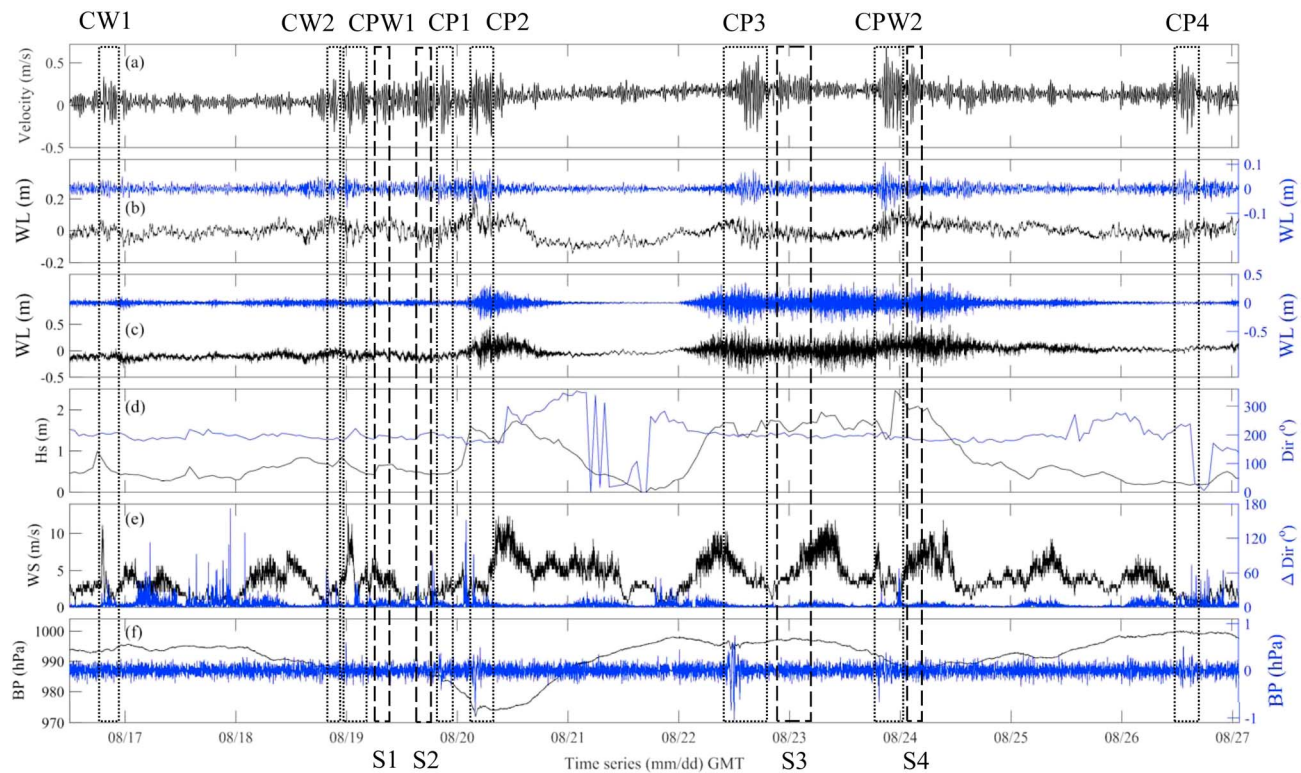


Figure 5. Time series of (a) velocities at A4; (b) water level (WL; raw data in black and 2-hr high-pass filtered in blue) at HM3; (c) same as (b) at HM5; (d) significant wave height (black) and wave direction (blue) at National Oceanic and Atmospheric Administration National Data Buoy Center buoy 45002; (e) wind speed (black) and 1-min variation in direction (blue) at KISQ; (f) barometric pressure (BP; raw data in black and 2-hr high-pass filtered in blue) at KISQ during August 2016. Dotted and dashed boxes identify meteotsunami and seiche events, respectively. C and S stand for a convective storm and a seiche event, respectively. P, W, and PW represent pressure driven ($P^* > 60\%$), wind driven ($W^* > 60\%$), and pressure and wind driven ($40\% < P^* < 60\%$ and $40\% < W^* < 60\%$), respectively. Number denotes a different event.

maintained a relatively constant direction. The wind speed increased from 4 to 10 m/s and from 7 to 10 m/s for the S3 and S4 events, respectively. Note that the direction of wind waves was observed from the northeast toward the southwest ($\sim 200^\circ$), propagating away from the MR during this period. As a result, the energy transfer from wind waves to lower frequency water level oscillations is expected to be negligible. Overall, eight meteotsunamis, driven by pressure and wind disturbances, and four seiches, driven by wind fluctuations in speed and direction, are identified. All these MIWLO events are associated with large velocity fluctuations.

4.2. MIWLO Causalities

Causes of the 12 large velocity events are revealed by the time-frequency spectral characteristics of pressure, wind speed, water level, and velocity through WPS and CWPS analysis. Specifically, the WPS of velocities, water level at HM3 and HM5, and wind and pressure at KISQ are shown in Figures 6a–6e, respectively. WPS for CW1 and CW2 events show that wind oscillated strongly between 32–128 min and 16–80 min, respectively (Figure 6d), while almost no energetic oscillations occurred in air pressure (Figure 6e). These wind oscillations coincided with energetic water level oscillations outside the MR between 128 and 256 min during CW1 and between 64 and 128 min during CW2 (Figure 6c), which excited or amplified higher frequency water level oscillations inside the harbor (Figure 6b). Specifically, energetic oscillations inside MR occurred between 20 and 40 min during CW1 and between 16 and 128 min during CW2 (Figure 6b). Meanwhile, there were apparent velocity fluctuations between 16 and 32 min inside MR during CW1 and CW2 events (Figure 6a). Overall, WPS of water level exhibits energetic oscillations in a wide range of frequencies. In contrast, WPS of velocities depicts a distinct spectral signature close to 26 min, the natural oscillation mode of the harbor (Linares et al., 2016). WPS analysis for the study period reveals that observed energetic velocity events coincide with energetic oscillations in air pressure and/or wind speed with periods below 120 min.

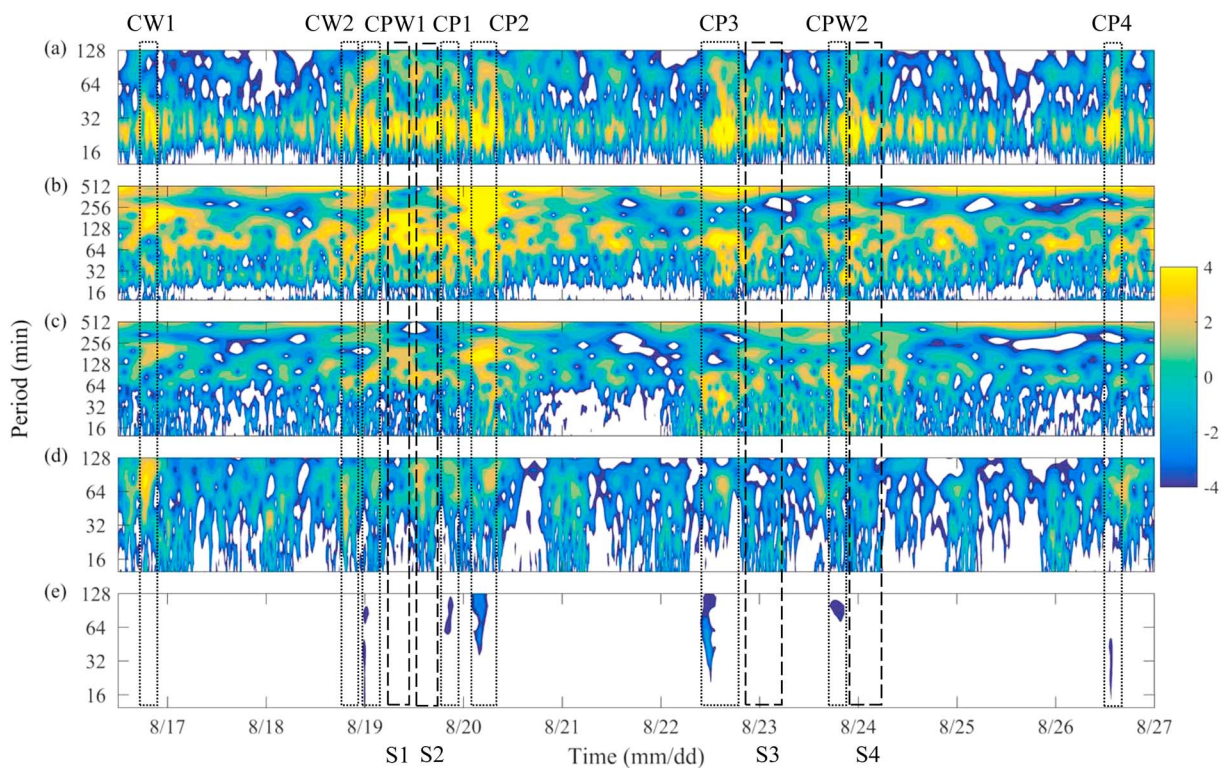


Figure 6. Wavelet power spectrum (WPS) of (a) velocities at A4; (b) water level at HM3; (c) water level at HM5; (d) wind speed; and (e) barometric pressure during August 2016. WPS is shown as the base 2 logarithm, and white swaths indicate that the logarithmic WPS is smaller than -4 .

The CWPS for velocities and water level at HM3 with atmospheric forcing at KISQ are depicted in Figures 7a–7d. For two of the meteotsunamis (CW1, CW2) and all four seiche events (S1, S2, S3, and S4), velocity and wind oscillated between 16 and 32 min. (Figure 7a). For the other six meteotsunamis (events CPW1, CPW2, CP1, CP2, CP3, and CP4), velocity oscillated with both wind and pressure from a few minutes to 2 hr (Figure 7b). The magnitudes of CWPS between velocity and atmospheric forcing are consistent with the percentages of wind and pressure dictated by pressure gradient and wind shear stress of the eight meteotsunami-causing atmospheric disturbances. Figures 7c and 7d show that the CWPS between water level and atmospheric disturbances are similar to those of large velocity and atmospheric disturbances. Nevertheless, the energy content of CWPS between water levels and atmospheric disturbances is somehow spreading wider, especially on 18, 25, and 26 August. One possible explanation is that according to the shallow water wave equations, velocity variations are about 10 times (acceleration of gravity) more sensitive than water level fluctuations, leading to a distinct signature in the CWPS. In comparison, it is suggested that velocity CWPS can be a better indicator of meteotsunamis and seiche events in estuaries. Overall, time-frequency analysis indicates that energetic high-frequency (period <2 hr) oscillations in both wind and pressure can cause meteotsunamis and seiches, thus driving large velocity events in estuaries. To the authors' knowledge, this is the first time that the CWPS are employed to reveal the relationship between the time-frequency content of causative atmospheric forcing and the resultant velocities of meteotsunamis.

4.3. Bottom Shear Stresses and Hydrodynamics

Characteristics of bottom shear stresses under MIWLO-dominated and river-dominated flow conditions are investigated here. For the eight meteotsunamis and four seiche events (MIWLO-dominated) during the study period (Figure 5a), large magnitude velocity fluctuations and strong flow reversals (negative velocities) were apparent. For the period of river-dominated flow over the MIWLOs, velocities tended to be positive with small fluctuations. For example, Figures 8a and 8d show time series of the bottom shear stress for 20 August and 21 August 2016, representing a MIWLO-dominated event (CP2) and a river-dominated event, respectively. During the CP2 event, bottom shear stresses fluctuated between -0.87 (negative indicating upstream) and

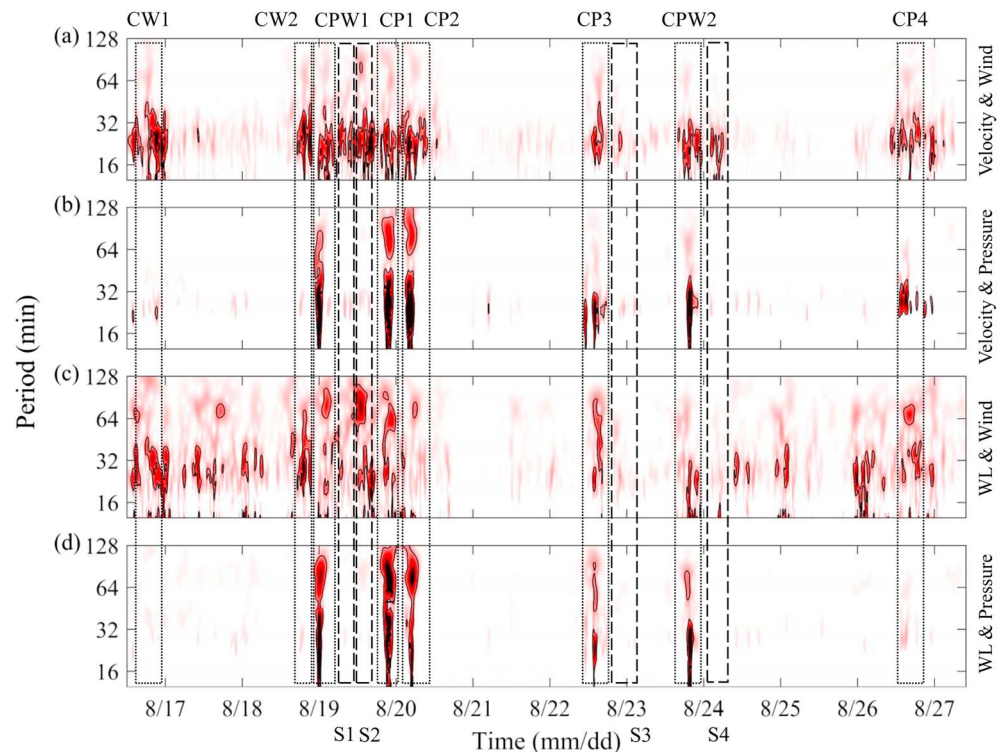


Figure 7. Cross-wavelet power spectra of (a) velocity and wind; (b) velocity and air pressure; (c) water level (WL) and wind; and (d) water level and air pressure normalized by the 95% confidence level for the corresponding red-noise spectrum at each scale (power relative to significant level) during August 2016. Air pressure and wind are obtained from the KISQ Automated Surface Observing System station, velocity from A4, and water level from HM3.

1.37 Pa (positive indicating downstream) with a mean value of 0.1 Pa, corresponding to depth-averaged velocity fluctuations between -0.37 and 0.47 m/s and a mean value of 0.08 m/s (Figure 8b). In contrast, during the river-dominated flow event, bottom shear stresses ranged between 0 and 0.3 Pa with a mean value of 0.07 Pa, associated with depth-average velocities up to 0.27 m/s and a mean value of 0.15 m/s (Figure 8d). In comparison, the mean bottom shear stress induced by MIWLOs was an order of magnitude larger than that induced by the river-dominated flow conditions due to the quadratic relationship between bottom shear stress and velocity. As a result, 48% of the time during CP2 event bottom shear stress was larger than the average critical shear stress threshold of 0.1 Pa, with 66% of these events being positive and 34% being negative. In contrast, there was only 18% of the time during the river-dominated event when the bottom shear stress exceeded the resuspension threshold. Overall, the number of sediment resuspension events are significantly larger under the MIWLO-dominated conditions, which can increase bottom shear stress by an order of magnitude and cause reversed shear. To the authors' knowledge, this is the first time that the meteotsunami-induced bottom shear stress is investigated and reported.

Hydrodynamics induced by MIWLOs in estuaries in the Great Lakes is analogous to tidal-induced hydrodynamics in oceans. The largest negative/positive velocities during the CP2 event (Figure 8b) were observed after water levels increased/decreased to the mean depth (Figure 8c). Zero velocities occurred when water level reaches local maximum or minimum. The time duration between largest negative/positive velocities was approximately of 26 min in the MR, consistent to the natural oscillation mode of the harbor (Linares et al., 2016). In comparison, water levels for the river-dominated flow conditions were lower than the mean (Figure 8f). Oscillation of velocities were apparent, but the magnitudes were small so that the resulting velocities were positive toward Lake Michigan, that is, no reversal flow (Figure 8e). Velocity profiles for interactions of river flow with MIWLOs are further examined here. Figure 9a shows the ensemble-averaged velocity profiles by ADCP for the positive maximum (black) and negative minimum (red) peaks normalized

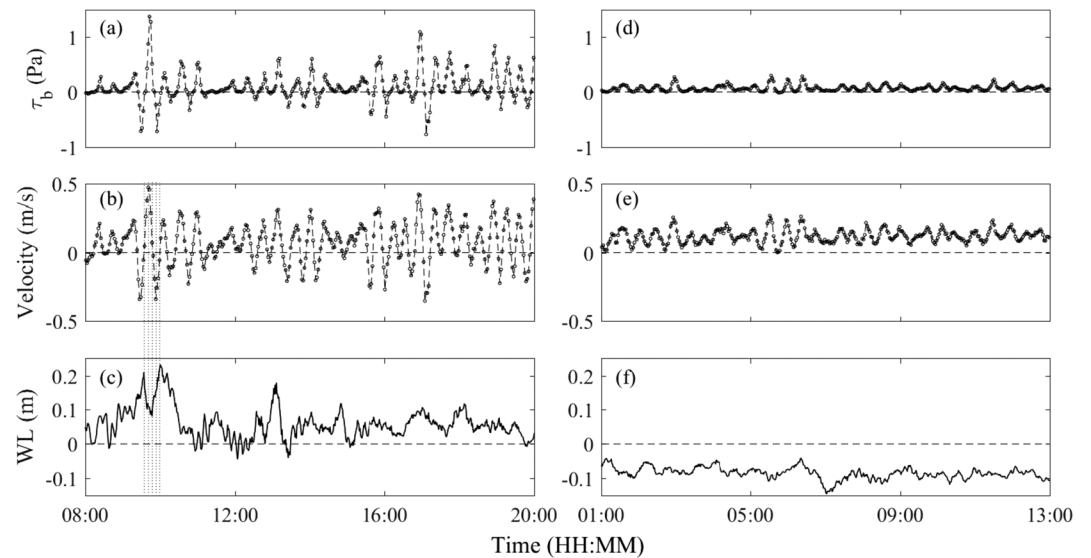


Figure 8. Bottom shear stress, depth average velocity, and water level (WL) at A4 during 20 August (a, b, c) and 21 August (d, e, f). Simultaneous occurrence of local maximum and minimum water levels with slowest velocities, and decrease/increase of water levels with maximum/minimum velocities during 20 August are depicted with dotted lines (b, c).

by the mean depth-averaged velocity over the period of the CP2 meteotsunami event on 20 August 2016. The velocity profiles in the lower part ($z < 0.84$ m) of the water column followed a logarithmic shape with $R^2 = 0.998$ and 0.997 for the maximum and minimum peaks, respectively. The estimated bed roughness is 0.0032 m with the standard deviation of 0.002 m. These results are consistent with other studies that measured velocity profiles under acceleration flows (Heathershaw & Langhorne, 1988; Kuo et al., 1996) and bed roughness over sandy sediments (Amos et al., 2010; Dyer, 1980). For the river-dominated condition on 21 August 2016, the ensemble-averaged velocity profile normalized by the mean depth-averaged velocity over a period of 12 hr exhibited a logarithmic shape in the lower 1.47 m of the flow with $R^2 = 0.996$ and 0.998 for maximum and minimum peaks, respectively. The profile throughout the water column closely resembled a power law, typically observed in wide open channels under uniform flow (Chanson, 2004). Furthermore, bed roughness during this period was 0.0031 m on average but showed a standard deviation

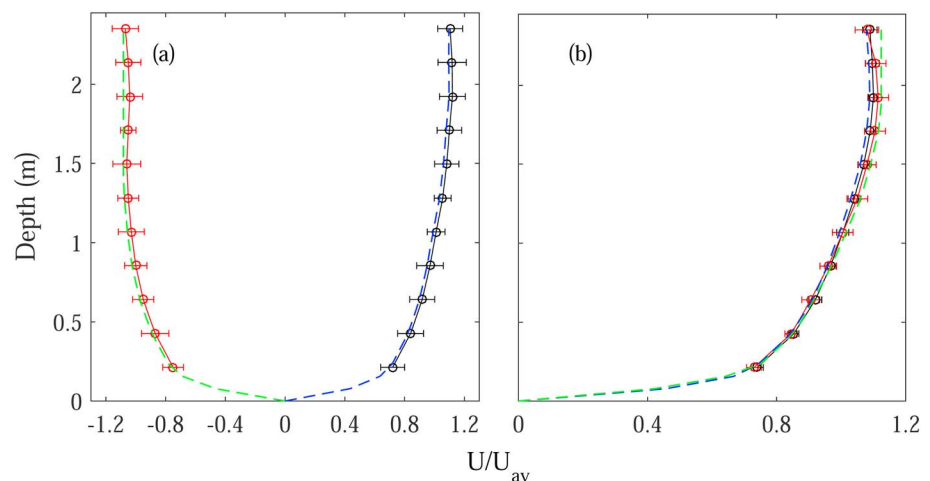


Figure 9. Observed (solid black and red) and modeled (dashed blue and green) ensemble-averaged velocity profiles for maximum (black and blue) and minimum (red and green) depth-averaged velocity peaks during (a) 20 August and (b) 21 August. Velocity profiles are normalized with respect to the mean depth-averaged velocities for each 12-hr period (U_{av}). Standard deviations of the normalized ensemble velocity at each measured height are also provided.

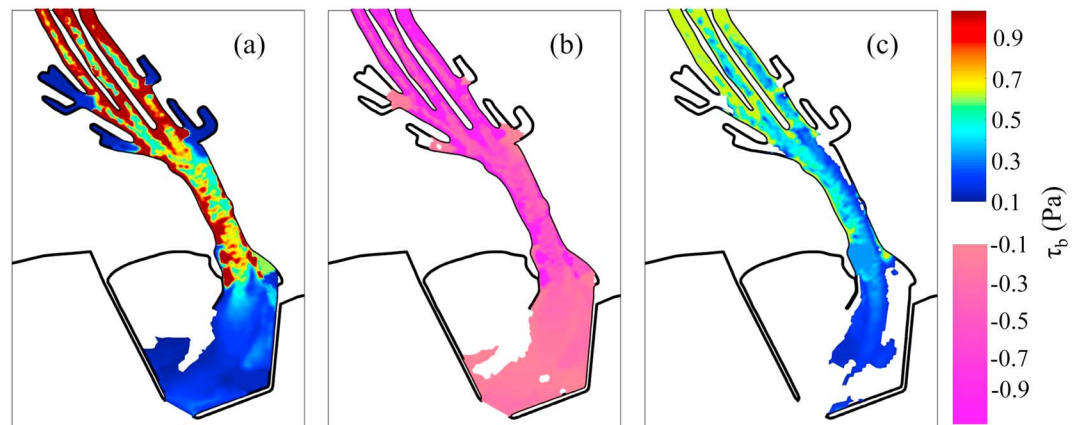


Figure 10. Maximum bottom shear stress maps during (a) downstream flow and (b) upstream flow on 20 August and during (c) downstream flow on 21 August. Locations where the maximum bottom shear stress was below the resuspension threshold of 0.1 Pa are kept white. In the main channel, upstream tributaries, and western harbor, bottom shear stress is defined as positive/negative when the projection of the bottom shear stress vector into the main axis of the main channel (148° from north) points toward downstream/upstream. For the center and eastern areas of the harbor, the projection axis connects the harbor mouth and the main channel (208° from north).

50% smaller (0.001 m) than that during the MIWLO-dominated CP2 event, likely due to the larger uniformity of the flow (Biron et al., 2004). Overall, the velocity profile during river-dominated flow conditions approximately followed the logarithmic law in half of the flow depth. The velocity profile caused by interaction of river flow and MIWLOs were altered so that the logarithmic law was valid in the lower 30% of the water column.

4.4. Spatial Variations of Maximum Bottom Shear Stresses

Maximum bottom shear stresses in the MR are calculated using the hydrodynamic model. Figures 10a and 10b show the maximum bottom shear stress maps for the positive flow directed downstream toward Lake Michigan and the negative flow directed upstream toward the MR, respectively, during the MIWLO-dominated event on 20 August 2016. Bottom shear stresses over 0.5 Pa appeared in the majority of the upstream narrow channels and downstream main channel in the MR, agreeing well with bottom shear stress estimates from ADCP observations. In contrast, in the harbor area bottom shear stresses were low (0.1–0.3 Pa), and bottom shear stresses below the resuspension threshold (0.1 Pa) were denoted to be white (Figure 10a). When the flow was reversed to travel to upstream, the magnitude of bottom shear stresses slightly decreased due to the interaction of the downstream river flow and the upstream flow induced by the meteotsunami (see Figure 10b). Overall, the bottom shear stresses under both the downstream and upstream flows during the MIWLO-dominated event were significantly larger than those during river-dominated flow conditions on 21 August 2016 (Figure 10c). The area below the critical resuspension threshold (0.1 Pa), denoted to be white, for the river-dominated flow conditions was even larger, suggesting that MIWLO-dominated flows, in comparison with river-dominated flows, do play an important role in sediment transport in the Great Lakes estuaries. Note that the river flows during the month of August in the MR are generally low. Large river flood flows (i.e., snow-melts during early spring and rainfall storms during summer or late fall) interacting with MIWLOs can dramatically alter magnitudes and patterns of bottom shear stresses in the MR, which will be discussed in the following sections.

5. Discussion

5.1. Validity of Bottom Shear Stress Estimate

Bottom shear stresses estimated by the hydrodynamic model with a LP formula is assessed here by comparing with those obtained with observations using the turbulent kinetic energy and direct covariance methodologies (Kim et al., 2000). Specifically, three-dimensional velocities were measured by a Nortek acoustic Doppler velocimeter (range: ± 4 m/s; accuracy ± 0.1 cm/s) at the same location A4 on 29 August 2012. Results show that average of bottom shear stress using turbulent kinetic energy, direct covariance, and the

LP methods are 0.019, 0.021, and 0.022 Pa with the associated 95% confidence intervals being ± 0.00342 , ± 0.00756 , and ± 0.00968 Pa, respectively. The corresponding confidence intervals are $\pm 18\%$, $\pm 36\%$, and $\pm 44\%$ of the individual estimated value, respectively. The LP method has the largest variability, in agreement with other studies in the literature (e.g., Biron et al., 2004; Kim et al., 2000; Wilcock, 1996). Overall, the LP method employed in the hydrodynamic model does reliably estimate bottom shear stresses caused by MIWLOs in the MR.

A LP formula with a drag coefficient and a bed roughness length z_0 (Wilcock, 1996) at the bottom computational cell (Zhang et al., 2016) is used to calculate bottom shear stress. Figure 9a shows the good comparison between the modeled velocity profiles and the observation profiles by the ADCPs at location A4 with RMSE of 0.019 m/s for the positive maximum (blue dashline) and 0.027 m/s for the negative minimum (green dashline) peaks of the CP2 event. Similar results for the river-dominated condition with RMSE of 0.017 and 0.012 m/s for the positive maximum (blue dashline) and minimum (green dashline) peaks are also seen in Figure 9b. The modeled velocity profiles approximate a LP near the bottom but differ from the logarithmic shape near the surface of the water column. This result is consistent to previous studies (Kuo et al., 1996; Soulsby & Dyer, 1981; Wilkinson, 1986) that velocity profiles can deviate 5–10% from the logarithmic shape during accelerated and decelerated flows such as tidal flows. Overall, the good agreement between modeled and observed velocity profiles validates the use of the hydrodynamic model to estimate bottom shear stress under MIWLO-dominated and river-dominated conditions.

5.2. Interactions Between MIWLOs and Flood Flows

Interactions between MIWLOs and river flood flows are common in Great Lakes estuaries (Bedford, 1992; Quinn, 1988; Sorensen et al., 2004; Trebitz, 2006). Based upon 15-year data, Bechle et al. (2016) revealed that the occurrence of meteotsunamis in Lake Michigan is higher during April and July. Specifically, meteotsunamis in northern Lake Michigan usually occur in the month of April, with a secondary peak in May and June (Bechle et al., 2015). The wave height of observed meteotsunamis in the Great Lakes reach 0.6 m with period ranging from 0.2 to ~ 2 hr (Bechle et al., 2015, 2016). Similar magnitudes with wave heights around 0.5–0.7 m were observed during the field campaign in 2012 (Linares et al., 2016). Based on the United States Geological Survey flow gage at the MR (https://waterdata.usgs.gov/nwis/uv?site_no=04056500), the largest flood flows usually occur during the spring melt in the MR with the mean maximum flood discharge of $170 \text{ m}^3/\text{s}$. As a result, interactions between spring floods and meteotsunamis occur annually at least.

The role of MIWLO-flood interactions on bottom shear stresses in the estuary is examined here. As shown previously in section 4.2, MIWLOs in the MR exhibit a strongest oscillation period of 26 min. We force the hydrodynamic model using a wave height of 0.6 m with a period of 26 min for MIWLOs and a discharge of $170 \text{ m}^3/\text{s}$. Figure 11 shows the map of magnitudes of maximum bottom shear stresses in the MR caused by the interactions of flood discharge with MIWLOs of positive flow directed downstream toward Lake Michigan (Figure 11a) and negative flow directed upstream toward the MR (Figure 11b), in comparison with that caused by flood discharge individually in Figure 11c. Three distinct spatial features are found. First, in the main river channels, maximum bottom shear stresses induced by the interaction of flood discharge and positive MIWLOs are above 13 Pa (Figure 11a), significantly larger than the 3.5 Pa induced by the flood discharge (Figure 11c). In contrast, maximum bottom shear stresses induced by the interaction of flood discharge and negative MIWLOs are below 1 Pa with values even below the sediment resuspension threshold of 0.1 Pa (denoted in white in Figure 11b). Second, in the downstream harbor, maximum bottom shear stresses at the center area of the harbor exhibit a similar spatial pattern like the main river channel except that the magnitudes are much smaller, for example, 3–6 Pa for Figure 11a and 0.5–2 Pa for Figure 11c. Specifically, maximum bottom shear stresses induced by the interaction of flood discharge and negative MIWLOs are all below 0.1 Pa, suggesting that no resuspension would occur. Third, at the eastern and western parts of the harbor and the four upstream tributaries where bottom shear stresses induced by the flood discharge are less than the resuspension threshold, interactions of the flood discharge and positive MIWLOs (Figure 11a) and negative MIWLOs (Figure 11b) yield the net velocity large enough to result in bottom shear stresses of ± 0.31 Pa on average, suggesting that MIWLOs are responsible for resuspension of sediments in these areas under a wide range of river discharge conditions. Overall, the interactions of MIWLOs and flood flows can yield nonlinear spatial patterns of maximum bottom shear stresses in the MR estuary. In particular, their interactions can significantly alter the bottom shear stresses in the main river channel. It is revealed that MIWLOs

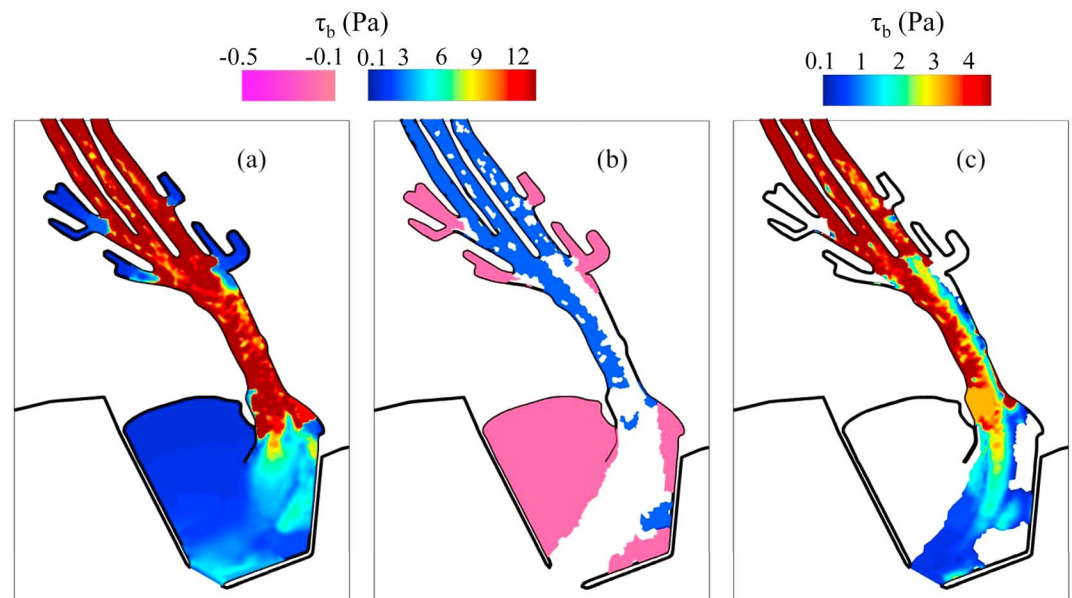


Figure 11. Maximum bottom shear stress maps during (a) downstream flow and (b) upstream flow induced by the interaction between mean of maximum spring flows ($Q = 170 \text{ m}^3/\text{s}$) and high-frequency MIWLOs with period of 26 min and wave height of 0.6 m. (c) Maximum bottom shear stress maps induced by mean of maximum spring flows ($Q = 170 \text{ m}^3/\text{s}$). Locations where the maximum bottom shear stress was below the resuspension threshold of 0.1 Pa are kept white. Positive and negative shear stresses follow the same definition as Figure 10.

are the principal resuspension mechanism in areas where flood flows individually do not cause resuspension, such as the western harbor area and the upstream tributaries, which have been the areas with recorded high concentration of contaminants in the MR.

5.3. MIWLO Asymmetry

Water level oscillation asymmetry can lead to asymmetry in velocities and subsequently to asymmetry on bottom shear stresses, which are critical to sediment transport processes in tidal estuaries (e.g., Dronkers, 1986). In the past, a great deal of effort has been paid to investigate the role of tidal asymmetry on sediment transport processes in ocean estuaries (e.g., Fry & Aubrey, 1990; Jewell et al., 2012; Lambiase, 1980). For example, the higher steepness of the wave crest leads to a shorter duration during a high tide than a low tide, thus causing velocity asymmetry with faster upstream velocities and slower downstream velocities in estuaries (Friedrichs & Aubrey, 1988; Nidzieko & Ralston, 2012; Speer & Aubrey, 1985). As a result, bottom shear stress is larger during a high tide than during a low tide. While MIWLOs in freshwater estuaries can be analogous to tides in the ocean, asymmetry features of MIWLOs in Great Lakes estuaries and their effects on sediment transport processes have yet to be examined.

Asymmetry of depth-averaged velocities and bottom shear stresses induced by MIWLOs in the MR, obtained from hydrodynamic modeling forced by MIWLOs with zero river flow, is examined here. Figure 12a shows the time series of velocities at the three locations, that is, main river channel, harbor, and tributary branches, shown in Figure 2b. Specifically, the maximum positive (directed downstream toward Lake Michigan) and negative (directed upstream toward the MR) velocities induced by MIWLOs are 1.27 and -1.41 m/s in the main river channel (red line in Figure 12a). Interestingly, the result is consistent to that in tidal estuaries in which a basin length is shorter than a tidal wave length (Rabinovich, 2009). Dronkers (1986) indicated that the asymmetry of tidal waves is induced by nonlinear propagation terms, $\delta(\eta u)/\delta x$ and $u\delta u/\delta x$, in the continuity and momentum equations as well as friction. As a result, the velocity asymmetry yields a longer duration for an ebb tide than that for a flood tide. In our study, the basin length of the MR is 1.7 km, smaller than 7.0 km for MIWLO wave length. The velocity asymmetry of MIWLOs at the main river channel also yields a longer duration of 13.5 min for positive velocities, in comparison with 12.5 min for negative velocities. Similar results with the asymmetry for velocity magnitudes and durations are also observed in areas outside the main

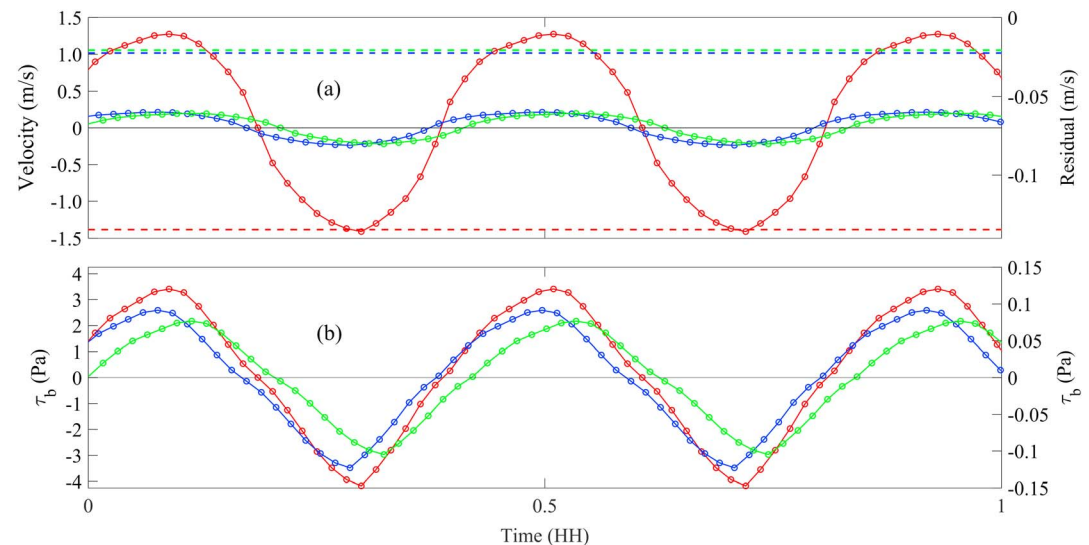


Figure 12. (a) Modeled depth-averaged velocities and (b) bottom shear stress at the three locations specified in Figure 2b (depicted as red, blue, and green dots) induced by high-frequency MIWLOs with period of 26 min and wave height of 0.6 m. Model output is shown every 1 min (circle markers). Dotted lines depict the residual of the velocity at the three locations. (b) Left y axis corresponds to the red line and right y axis corresponds to the blue and green lines.

channel, that is, the harbor (blue line) and tributary branches (green line) in Figure 12a, indicating that during MIWLOs the feature of asymmetry occurs throughout the whole estuary. At last, the time-averaged velocities over a positive and negative cycle, that is, residuals, at the main river channel, harbor, and tributary branch are -0.14 , -0.022 , and -0.02 m/s, respectively, confirming that MIWLOs play an important role in affecting flushing time of freshwater estuaries in the Great Lakes.

Asymmetry of bottom shear stress is magnified due to a nonlinear quadratic dependence on velocity. Figure 12b shows the time series of bottom shear stresses at the main river channel (red line) varying from the maximum 3.41 Pa to the minimum -4.17 Pa, which can be of importance to critical erosion shear stress at lower depth due to consolidation (Hayter, 1986; Lee et al., 2004) or affect net bottom sediment erosion rates (Fry & Aubrey, 1990; Liu et al., 2009). In other words, transport of bottom sediments out of MR to Lake Michigan can be smaller than that into the MR from Lake Michigan, yielding the net transport (or sediment residue) toward the MR. This asymmetry in bottom shear stresses also occurs in areas where the bottom shear stress induced by MIWLOs is close to the sediment resuspension threshold (Partheniades, 2009; Van Rijn, 1993). For instance, in the western harbor and upstream tributary of the MR (see green and blue dots in Figure 2b, respectively), the time series of bottom shear stresses induced by MIWLOs (green and blue in Figure 12b) exceeds the resuspension threshold (0.1 Pa) when velocities are negative but falls short of the threshold when velocities are positive, thus causing a residual upstream sediment transport. As a result, residence times of sediments located in the western harbor and upstream tributary are larger than those in the rest of the MR estuary. Overall, results reveal that asymmetry of bottom shear stresses and velocities induced by observed MIWLOs in fresh water Great Lakes estuaries can significantly alter the spatial pattern of sediment resuspension and transport. As far as the authors are aware, this is the first time that the importance of MIWLO asymmetry in the residence time of contaminated sediments in Great Lakes AOC is reported. Note that this study only addresses the velocity nonlinearity induced MIWLOs asymmetry. Further study should consider the role of interactions of multifrequency MIWLOs and river discharge on sediment settling and erosion lags (Partheniades, 2009; Postma, 1961; Van Straaten & Kuenen, 1958) and residuals sediment transport (Hoitink et al., 2003; Hoitink & Jay, 2016).

6. Conclusions

In this paper, the role of MIWLOs and river floods on bottom shear stresses in a freshwater estuary in the Great Lakes is investigated. Results show that both moving atmospheric disturbances and changes in wind speed and direction can generate MIWLOs. CWPS reveal causative relationship between the time-frequency content

of atmospheric forcing and the resultant velocities of meteotsunamis. MIWLO-dominated conditions can increase bottom shear stress by an order of magnitude in comparison with river-dominated flow conditions. Furthermore, bottom shear stresses under both the downstream and upstream flows during the MIWLO-dominated event were significantly larger than those during river-dominated conditions, suggesting that MIWLOs play an important role in sediment transport in freshwater estuaries in the Great Lakes. The role of MIWLO-flood interactions on bottom shear stresses in the MR is revealed. The interactions of MIWLOs and flood flows can yield nonlinear spatial patterns of maximum bottom shear stresses in the MR estuary. In particular, their interactions can significantly alter the bottom shear stresses in the main river channel. MIWLOs are revealed to be the principal resuspension mechanism in areas where flood flows individually do not cause resuspension, such as the western harbor area and the upstream tributaries, which have been the areas with recorded high concentration of contaminants in the MR. Asymmetry of velocities and bottom shear stresses induced by MIWLOs in the MR is also studied and confirmed, consistent to those findings in tidal estuaries in the ocean. MIWLOs asymmetry in freshwater Great Lakes estuaries can significantly alter the spatial pattern of sediment resuspension and transport. Overall, this paper fills important knowledge gaps in the role of MIWLOs on sediment transport in enclosed basin estuaries, thus providing essential information for management and remediation processes of nontidal estuaries and Great Lakes AOCs.

Acknowledgments

This work was supported in part by the Great Lakes Restoration Initiative, Cooperative Institute for Great Lakes Research, and the University of Wisconsin Sea Grant Institute. The authors would like to thank David Schwab at the Graham Sustainability Institute, University of Michigan for his encouragement on the initiation of this project. In addition, his valuable discussion on meteotsunamis research in the Great Lakes is greatly acknowledged here. We also would like to acknowledge Ying-Ting (Kevin) Lin for his assistance on field work and sediment erosion lab experiments and analysis during the period of 2012–2013. The data presented in this study can be accessed through http://homepages.cae.wisc.edu/~chinwu/MR_Data.html.

References

- Amos, C. L., Villatoro, M., Helsby, R., Thompson, C. E. L., Zaggia, L., Umgieser, G., et al. (2010). The measurement of sand transport in two inlets of Venice lagoon, Italy. *Estuarine, Coastal and Shelf Science*, 87(2), 225–236. <https://doi.org/10.1016/j.ecss.2009.05.016>
- Anderson, E. J., Bechle, A. J., Wu, C. H., Schwab, D. J., Mann, G. E., & Lombardy, K. A. (2015). Reconstruction of a meteotsunami in Lake Erie on 27 May 2012: Roles of atmospheric conditions on hydrodynamic response in enclosed basins. *Journal of Geophysical Research: Oceans*, 120, 8020–8038. <https://doi.org/10.1002/2015JC010883>
- As-Salek, J. A., & Schwab, D. J. (2004). High-frequency water level fluctuations in Lake Michigan. *Journal of Waterway, Port, Coastal, and Ocean Engineering*, 130(1), 45–53. [https://doi.org/10.1061/\(ASCE\)0733-950X](https://doi.org/10.1061/(ASCE)0733-950X)
- ASTM D-1587-08 (2007). Standard practice for thin-walled tube sampling of soils for geotechnical purposes, American Society for Testing and Materials.
- ASTM D-2487-98 (2000). Standard practice for classification of the soil for engineering purposes (unified soil classification system), American Society for Testing and Materials.
- Bechle, A. J., Kristovich, D. A. R., & Wu, C. H. (2015). Meteotsunami occurrences and causes in Lake Michigan. *Journal of Geophysical Research: Oceans*, 120, 8422–8438. <https://doi.org/10.1002/2015JC011317>
- Bechle, A. J., & Wu, C. H. (2014). The Lake Michigan meteotsunamis of 1954 revisited. *Natural Hazards*, 74(1), 155–177. <https://doi.org/10.1007/s11069-014-1193-5>
- Bechle, A. J., Wu, C. H., Kristovich, D. A. R., Anderson, E. J., Schwab, D. J., & Rabinovich, A. B. (2016). Meteotsunamis in the Laurentian Great Lakes. *Scientific Reports*, 6(1). <https://doi.org/10.1038/srep37832>
- Bedford, K. W. (1992). The physical effects of the Great Lakes on tributaries and wetlands. *Journal of Great Lakes Research*, 18(4), 571–589. [https://doi.org/10.1016/S0380-1330\(92\)71323-9](https://doi.org/10.1016/S0380-1330(92)71323-9)
- Bedford, K. W., & Abdelrhman, M. (1987). Analytical and experimental studies of the bottom boundary layer and their applicability to near-bottom transport in Lake Erie. *Journal of Great Lakes Research*, 13, 628–648. [https://doi.org/10.1016/S0380-1330\(87\)71678-5](https://doi.org/10.1016/S0380-1330(87)71678-5)
- Bertin, X., Bruneau, N., Breilh, J., Fortunato, A., & Karpytchev, M. (2011). Importance of wave age and resonance in storm surges: The case Xynthia, Bay of Biscay. *Ocean Modelling*, 42, 16–30. <https://doi.org/10.1016/j.ocemod.2011.11.001>
- Biron, P. M., Robson, C., Lapointe, M. F., & Gaskin, S. J. (2004). Comparing different methods of bottom shear stress estimates in simple and complex flow fields. *Earth Surface Processes and Landforms*, 29(11), 1403–1415. <https://doi.org/10.1002/esp.1111>
- Blayo, E., & Debreu, L. (2005). Revisiting open boundary conditions from the point of view of characteristic variables. *Ocean Modelling*, 9(3), 231–252. <https://doi.org/10.1016/j.ocemod.2004.07.001>
- Cai, H., Savenije, H. H. G., & Toffolon, M. (2014). Linking the river to the estuary: influence of river discharge on tidal damping. *Hydrology and Earth System Sciences*, 18, 287–304. <https://doi.org/10.5194/hess-18-287-2014>
- Candella, R. N. (2009). Meteorologically induced strong seiches observed at Arraial do Cabo, RJ Brazil. *Physics and Chemistry of the Earth*, 34(17–18), 989–997. <https://doi.org/10.1016/j.pce.2009.06.007>
- Chanson, H. (2004). *The hydraulics of open channel flow: An introduction*, vol. xlvii, 2nd ed. Oxford, Burlington, MA: Elsevier, Butterworth-Heinemann; 585 p, [16] of Plates.
- Cho, K. H., Wang, H. V., Shen, J., Valle-Levinson, A., & Teng, Y. C. (2012). A modeling study on the response of the Chesapeake Bay to hurricane events of Floyd and Isabel. *Ocean Modelling*, 49, 22–46. <https://doi.org/10.1016/j.ocemod.2012.02.005>
- Daubechies, I. (1990). The wavelet transform, time-frequency localization and signal analysis. *IEEE Transactions on Information Theory*, 36(5), 961–1005. <https://doi.org/10.1109/18.57199>
- Defant, A. (1961). *Physical oceanography*. Oxford: Pergamon Press.
- Derecki, J. A., & Quinn, F. H. (1990). Comparison of measured and simulated flows during the 15 December 1987 Detroit River flow reversal. *Journal of Great Lakes Research*, 16(3), 426–435. [https://doi.org/10.1016/S0380-1330\(90\)71435-9](https://doi.org/10.1016/S0380-1330(90)71435-9)
- Dey, S. (1999). Sediment threshold. *Applied Mathematical Modelling*, 23(5), 399–417. [https://doi.org/10.1016/S0307-904X\(98\)10081-1](https://doi.org/10.1016/S0307-904X(98)10081-1)
- Dronkers, J. (1986). Tidal asymmetry and estuarine morphology. *Netherlands Journal of Sea Research*, 20(2–3), 117–131. [https://doi.org/10.1016/0077-7579\(86\)90036-0](https://doi.org/10.1016/0077-7579(86)90036-0)
- Dyer, K. R. (1980). Velocity profiles over a rippled bed and the threshold of movement of sand. *Estuarine, Coastal and Marine Science*, 10(2), 181–199. [https://doi.org/10.1016/S0302-3524\(80\)80057-0](https://doi.org/10.1016/S0302-3524(80)80057-0)
- Friedrichs, C. T., & Aubrey, D. G. (1988). Non-linear tidal distortion in shallow well-mixed estuaries: A synthesis. *Estuarine, Coastal and Shelf Science*, 27, 521–545. [https://doi.org/10.1016/0272-7714\(88\)90082-0](https://doi.org/10.1016/0272-7714(88)90082-0)

- Fry, V. A., & Aubrey, D. G. (1990). Tidal velocity asymmetry and bedload transport in shallow embayments. *Estuarine, Coastal and Shelf Science*, 30(5), 453–473. [https://doi.org/10.1016/0272-7714\(90\)90067-2](https://doi.org/10.1016/0272-7714(90)90067-2)
- Gardner, J. T., English, M. C., & Prowse, T. D. (2006). Wind-forced seiche events on Great Slave Lake: Hydrologic implications for the Slave River Delta, NWT, Canada. *Hydrological Processes*, 20(19), 4051–4072. <https://doi.org/10.1002/hyp.6419>
- Godin, G. (1999). The Propagation of Tides up Rivers With Special Considerations on the Upper Saint Lawrence River. *Estuarine, Coastal and Shelf Science*, 48, 307–324. <https://doi.org/10.1006/ecss.1998.0422>
- Green, M. O. (1992). Spectral estimates of bed shear stress at subcritical Reynolds numbers in a tidal boundary layer. *Journal of Physical Oceanography*, 22(8), 903–917. [https://doi-org.ezproxy.library.wisc.edu/10.1175/1520-0485\(1992\)022<0903:SEOBSS>2.0.CO;2](https://doi-org.ezproxy.library.wisc.edu/10.1175/1520-0485(1992)022<0903:SEOBSS>2.0.CO;2)
- Green, M. O., & Coco, G. (2014). Review of wave-driven sediment resuspension and transport in estuaries. *Reviews of Geophysics*, 52, 77–117. <https://doi.org/10.1002/2013RG000437>
- Greenspan, H. P. (1956). The generation of edge waves by moving pressure disturbances. *Journal of Fluid Mechanics*, 1(06), 574–592. <https://doi.org/10.1017/S002211205600038X>
- Grinsted, A., Moore, J., & Jevrejeva, S. (2004). Application of the cross wavelet transform and wavelet coherence to geophysical time series. *Nonlinear Processes in Geophysics*, 11(5/6), 561–566. <https://doi.org/10.5194/npg-11-561-2004>
- Hayter, E. J. (1986). Estuarial bed model. In *Estuarine cohesive sediment dynamics* (pp. 326–359). New York: Springer-Verlag. https://doi.org/10.1007/978-1-4612-4936-8_16
- Heathershaw, A. D., & Langhorne, D. N. (1988). Observations of near-bed velocity profiles and seabed roughness in tidal currents flowing over sandy gravels. *Estuarine, Coastal and Shelf Science*, 26(5), 459–482. [https://doi.org/10.1016/0272-7714\(88\)90001-7](https://doi.org/10.1016/0272-7714(88)90001-7)
- Hlevca, B., Wells, M. G., & Parker, S. (2015). Amplification of long-period waves in shallow coastal embayments of the Great Lakes. *Environmental Fluid Mechanics*, 15(6), 1181–1213. <https://doi.org/10.1007/s10652-015-9406-3>
- Hoitink, A. J. F., Hoekstra, P., & van Maren, D. S. (2003). Flow asymmetry associated with astronomical tides: Implications for the residual transport of sediment. *Journal of Geophysical Research*, 108(C10), 3315. <https://doi.org/10.1029/2002JC001539>
- Hoitink, A. J. F., & Jay, D. A. (2016). Tidal river dynamics: Implications for deltas. *Reviews of Geophysics*, 54, 240–272. <https://doi.org/10.1002/2015RG000507>
- International Joint Commission (1978). The water quality agreement between the United States and Canada on Great Lakes water. International Joint Commission, Windsor, Ontario.
- International Joint Commission (1989). Revised Great Lakes water quality agreement of 1978 as amended by protocol signed November 18, 1987. International Joint Commission, Washington, DC.
- Jewell, S. A., Walker, D. J., & Fortunato, A. B. (2012). Tidal asymmetry in a coastal lagoon subject to a mixed tidal regime. *Geomorphology*, 138(1), 171–180. <https://doi.org/10.1016/j.geomorph.2011.08.032>
- Kim, S. C., Friedrichs, C. T., Maa, J. P. Y., & Wright, L. D. (2000). Estimating bottom stress in tidal boundary layer from acoustic Doppler velocimeter data. *Journal of Hydraulic Engineering*, 126(6), 399–406. [https://doi.org/10.1061/\(ASCE\)0733-9429\(2000\)126:6\(399\)](https://doi.org/10.1061/(ASCE)0733-9429(2000)126:6(399))
- Kuo, A. Y., Shen, J., & Hamrick, J. M. (1996). Effect of acceleration on bottom shear stress in tidal estuaries. *Journal of Waterway, Port, Coastal, and Ocean Engineering*, 122(2), 75–83. [https://doi.org/10.1061/\(ASCE\)0733-950X\(1996\)122:2\(75\)](https://doi.org/10.1061/(ASCE)0733-950X(1996)122:2(75))
- Lambiasi, J. L. (1980). Hydraulic control of grain-size distributions in a macrotidal estuary. *Sedimentology*, 27(4), 433–446. <https://doi.org/10.1111/j.1365-3091.1980.tb01192.x>
- Lee, C., Wu, C. H., & Hoopes, J. A. (2004). Automated sediment erosion testing system using digital imaging. *Journal of Hydraulic Engineering*, 130(8), 771–782. [https://doi.org/10.1061/\(ASCE\)0733-9429\(2004\)130:8\(771\)](https://doi.org/10.1061/(ASCE)0733-9429(2004)130:8(771))
- Lin, Y. T., & Wu, C. H. (2013). Response of bottom sediment stability after carp removal in a small lake. *Annales de Limnologie - International Journal of Limnology*, 49(03), 157–168.
- Lin, Y. T., & Wu, C. H. (2014). A field study of nearshore environmental changes in response to newly-built coastal structures in Lake Michigan. *Journal of Great Lakes Research*, 40(1), 102–114. <https://doi.org/10.1016/j.jglr.2013.12.013>
- Lin, Y. T., Wu, C. H., Fratta, D., & Kung, K. J. S. (2010). An integrated acoustic and electromagnetic wave-based technique to estimate sub-bottom sediment properties in a freshwater environment. *Near Surface Geophysics*, 8(1730), 213–221. <https://doi.org/10.3997/1873-0604.2010006>
- Linares, Á., Bechle, A. J., & Wu, C. H. (2016). Characterization and assessment of the meteotsunami hazard in northern Lake Michigan. *Journal of Geophysical Research: Oceans*, 121, 7141–7158. <https://doi.org/10.1002/2016JC011979>
- Liu, W. C., Lee, C. H., Wu, C. H., & Kimura, N. (2009). Modeling diagnosis of suspended sediment transport in tidal estuarine system. *Environmental Geology*, 57(7), 1661–1673. <https://doi.org/10.1007/s00254-008-1448-0>
- Liu, Z., & Gan, J. (2016). Open boundary conditions for tidally and subtidally forced circulation in a limited-area coastal model using the Regional Ocean Modeling System (ROMS). *Journal of Geophysical Research: Oceans*, 121, 6184–6203. <https://doi.org/10.1002/2016JC011975>
- Lueck, R. G., & Lu, Y. (1996). The logarithmic layer in a tidal channel. *Continental Shelf Research*, 17(14), 1785–1801. [https://doi.org/10.1016/S0278-4343\(97\)00049-6](https://doi.org/10.1016/S0278-4343(97)00049-6)
- McLaren, P., & Singer, J. (2008). Sediment transport and contaminant behavior in the Buffalo River, New York: Implications for river management. *Journal of Coastal Research*, 24(4), 954–968. <https://doi.org/10.2112/06-0802.1>
- Miller, M. C., McCave, I. N., & Komar, P. D. (1977). Threshold of sediment motion under unidirectional currents. *Sedimentology*, 24(4), 507–527. <https://doi.org/10.1111/j.1365-3091.1977.tb00136.x>
- Monserat, S., Vilibić, I., & Rabinovich, A. B. (2006). Meteotsunamis: Atmospherically induced destructive ocean waves in the tsunami frequency band. *Natural Hazards and Earth System Sciences*, 6(6), 1035–1051. <https://doi.org/10.5194/nhess-6-1035-2006>
- Nidzieko, N. J., & Ralston, D. K. (2012). Tidal asymmetry and velocity skew over tidal flats and shallow channels within a macrotidal river delta. *Journal of Geophysical Research*, 117, C03001. <https://doi.org/10.1029/2011JC007384>
- Partheniades, E. (2009). *Cohesive sediments in open channels: Erosion, transport and deposition* (p. 357). New York: Elsevier.
- Pattiaratchi, C., & Wijeratne, E. M. S. (2015). Are meteotsunamis an underrated hazard? *Philosophical Transactions of the Royal Society A*, 373(2053). <https://doi.org/10.1098/rsta.2014.0377>
- Pinto, L., Fortunato, A. B., Zhang, Y., Oliveira, A., & Sancho, F. E. P. (2012). Development and validation of a three-dimensional morphodynamic modelling system for non-cohesive sediments. *Ocean Modelling*, 57–58, 1–14. <https://doi.org/10.1016/j.ocemod.2012.08.005>
- Postma, H. (1961). Transport and accumulation of suspended matter in the Dutch Wadden Sea. *Netherlands Journal of Sea Research*, 1(1–2), 148–190. [https://doi.org/10.1016/0077-7579\(61\)90004-7](https://doi.org/10.1016/0077-7579(61)90004-7)
- Proudman, J. (1929). The effects on the sea of changes in atmospheric pressure. *Geophysical Supplement: Monthly Notices of the Royal Astronomical Society*, 2(4), 197–209. <https://doi.org/10.1111/j.1365-246X.1929.tb05408.x>
- Quinn, F. H. (1988). Detroit River flow reversals. *Journal of Great Lakes Research*, 14(4), 383–387. [https://doi.org/10.1016/S0380-1330\(88\)71570-1](https://doi.org/10.1016/S0380-1330(88)71570-1)

- Rabinovich, A. B. (2009). Seiches and harbor oscillations, in: *Handbook of coastal and ocean engineering*, edited by Kim, Y.C. World Scientific Publishing Company, Singapore, 193–236. https://doi.org/10.1142/9789812819307_0009
- Rabinovich, A. B., & Monserrat, S. (1996). Meteorological tsunamis near the Balearic and Kuril Islands: Descriptive and statistical analysis. *Natural Hazards*, 13(1), 55–90. <https://doi.org/10.1007/BF00156506>
- Rao, D. B., Mortimer, C. H., & Schwab, D. J. (1976). Surface normal modes of Lake Michigan: Calculations compared with spectra of observed water level fluctuations. *Journal of Physical Oceanography*, 6(4), 575–588. [https://doi.org/10.1175/1520-0485\(1976\)006<0575:SNMOLM>2.0.CO;2](https://doi.org/10.1175/1520-0485(1976)006<0575:SNMOLM>2.0.CO;2)
- Rueda, F. J., & Cowen, E. A. (2005). The residence time of a freshwater embayment connected to a large lake. *Limnology and Oceanography*, 50(5), 1638–1653. <https://doi.org/10.4319/lo.2005.50.5.1638>
- Sasaki, Y., Gu, P., & Yan, L. (1955). A fundamental study of the numerical prediction based on the variational principle. *Journal of the Meteorological Society of Japan*, 33(6), 262–275. https://doi.org/10.2151/jmsj1923.33.6_262
- Schneider, A. R., Eadie, B. J., & Baker, J. E. (2002). Episodic particle transport events controlling PAH and PCB cycling in Grand Traverse Bay, Lake Michigan. *Environmental Science and Technology*, 36(6), 1181–1190. <https://doi.org/10.1021/es011262j>
- Schwab, D. J. (1978). Simulation and forecasting of Lake Erie storm surges. *Monthly Weather Review*, 106(10), 1476–1487. [https://doi.org/10.1175/1520-0493\(1978\)106<1476:SAFOLE>2.0.CO;2](https://doi.org/10.1175/1520-0493(1978)106<1476:SAFOLE>2.0.CO;2)
- Seiler, U. (1993). Estimation of open boundary conditions with the Adjoint method. *Journal of Geophysical Research*, 98, 855–870. <https://doi.org/10.1029/93JC02376>
- Šepić, J., Vilibić, I., & Monserrat, S. (2016). Quantifying the probability of meteotsunami occurrence from synoptic atmospheric patterns. *Geophysical Research Letters*, 43, 10,377–10,384. <https://doi.org/10.1002/2016GL070754>
- Shields, A. (1936). Anwendung der Ähnlichkeitsmechanik und der Turbulenzforschung auf die Geschiebcbewegung; In Mitteilungen der Preussischen Versuchsanstalt für Wasserbau und Schiffbau, Heft 26.
- Shulman, I., Lewis, J. K., Blumberg, A. F., & Kim, B. N. (1998). Optimized boundary conditions and data assimilation with application to the M2 tide in the Yellow Sea. *Journal of Atmospheric and Oceanic Technology*, 15(4), 1066–1071. [https://doi.org/10.1175/1520-0426\(1998\)015<1066:OBCADA>2.0.CO;2](https://doi.org/10.1175/1520-0426(1998)015<1066:OBCADA>2.0.CO;2)
- Shvidchenko, A. B., Pender, G., & Hoey, T. B. (2001). Critical shear stress for incipient motion of sand/gravel streambeds. *Water Resources Research*, 37, 2273–2283. <https://doi.org/10.1029/2000WR000036>
- Singer, J., Atkinson, J., Manley, P., & McLaren, P. (2008). Understanding sediment dynamics using geological and engineering approaches: A case study of the Buffalo River area of concern, Buffalo, New York. *International Journal of River Basin Management*, 6(1), 31–40. <https://doi.org/10.1080/15715124.2008.9635335>
- Sorensen, J., Sydor, M., Huls, H., & Costello, M. (2004). Analyses of Lake Superior seiche activity for estimating effects on pollution transport in the St. Louis river estuary under extreme conditions. *Journal of Great Lakes Research*, 30(2), 293–300. [https://doi.org/10.1016/S0380-1330\(04\)70347-0](https://doi.org/10.1016/S0380-1330(04)70347-0)
- Soulsby, R. L., & Dyer, K. R. (1981). The form of the near-bed velocity profile in a tidally accelerating flow. *Journal of Geophysical Research*, 86, 8067–8074. <https://doi.org/10.1029/JC086iC09p08067>
- Speer, P. E., & Aubrey, D. G. (1985). A study of non-linear tidal propagation in shallow inlet/estuarine systems part II: Theory. *Estuarine, Coastal and Shelf Science*, 21, 207–224. [https://doi.org/10.1016/0272-7714\(85\)90097-6](https://doi.org/10.1016/0272-7714(85)90097-6)
- Tanaka, I. (2010). Atmospheric pressure-wave bands around a cold front resulted in a meteotsunami in the East China Sea in February 2009. *Natural Hazards and Earth System Sciences*, 10(12), 2599–2610. <https://doi.org/10.5194/nhess-10-2599-2010>
- Torrence, C., & Compo, G. P. (1998). A practical guide to wavelet analysis. *Bulletin of the American Meteorological Society*, 79(1), 61–78. [https://doi.org/10.1175/1520-0477\(1998\)079<0061:APGTWA>2.0.CO;2](https://doi.org/10.1175/1520-0477(1998)079<0061:APGTWA>2.0.CO;2)
- Trebitz, A. S. (2006). Characterizing seiche and tide-driven daily water level fluctuations affecting coastal ecosystems of the Great Lakes. *Journal of Great Lakes Research*, 32(1), 102–116. [https://doi.org/10.3394/0380-1330\(2006\)32\[102:CSATDW\]2.0.CO;2](https://doi.org/10.3394/0380-1330(2006)32[102:CSATDW]2.0.CO;2)
- Trebitz, A. S., Morrice, J. A., & Cotter, A. M. (2002). Relative role of lake and tributary in hydrology of Lake Superior coastal wetlands. *Journal of Great Lakes Research*, 28(2), 212–227. [https://doi.org/10.1016/S0380-1330\(02\)70578-9](https://doi.org/10.1016/S0380-1330(02)70578-9)
- Van Rijn, L. C. (1993). *Principles of sediment transport in rivers, estuaries and coastal seas*. Amsterdam: Aqua.
- Van Straaten, L., & Kuenen, P. (1958). Tidal action as a cause of clay accumulation. *Journal of Sedimentary Petrology*, 28, 406–413.
- Vilibić, I., Domijan, N., Orlić, M., Leder, N., & Pasarić, M. (2004). Resonant coupling of a traveling air-pressure disturbance with the east Adriatic coastal waters. *Journal of Geophysical Research*, 109, C10001. <https://doi.org/10.1029/2004JC002279>
- Vilibić, I., Monserrat, S., Rabinovich, A. B., & Mihanović, H. (2008). Numerical modelling of the destructive meteotsunami of 15 June, 2006 on the coast of the Balearic Islands. *Pure and Applied Geophysics*, 165(11–12), 2169–2195. <https://doi.org/10.1007/s00024-008-0426-5>
- Wang, D., Qiang, L., & Lv, X. (2014). A study on bottom friction coefficient in the Bohai, Yellow, and East China Sea. *Mathematical Problems in Engineering*, 2014, 1–7. <https://doi.org/10.1155/2014/432529>
- Wang, X. H. (2002). Tide-induced sediment resuspension and the bottom boundary layer in an idealized estuary with a muddy bed. *Journal of Physical Oceanography*, 32(11), 3113–3131. [https://doi.org/10.1175/1520-0485\(2002\)032<3113:TISRAT>2.0.CO;2](https://doi.org/10.1175/1520-0485(2002)032<3113:TISRAT>2.0.CO;2)
- Wells, M. G., & Sealock, L. (2009). Summer water circulation in Frenchman's Bay, a shallow coastal embayment connected to Lake Ontario. *Journal of Great Lakes Research*, 35(4), 548–559. <https://doi.org/10.1016/j.jglr.2009.08.009>
- Werner, S. R., Beardsley, R. C., Lentz, S. J., Hebert, D. L., & Oakey, N. S. (2003). Observations and modeling of the tidal bottom boundary layer on the southern flank of Georges Bank. *Journal of Geophysical Research*, 108(C11), 8005. <https://doi.org/10.1029/2001JC001271>
- Wilcock, P. R. (1996). Estimating local bottom shear stress from velocity observations. *Water Resources Research*, 32, 3361–3366. <https://doi.org/10.1029/96WR02277>
- Wilkinson, R. H. (1986). Variation of roughness length of a mobile sand bed in a tidal flow. *Geo-Marine Letters*, 5(4), 231–239. <https://doi.org/10.1007/BF02233808>
- Wright, L. D. (1989). Benthic boundary layers of estuarine and coastal environments. *Reviews in Aquatic Sciences*, 1(1), 75–95.
- Zhang, Y., & Baptista, A. M. (2008). SELFE: A semi-implicit Eulerian-Lagrangian finite-element model for cross-scale ocean circulation. *Ocean Modelling*, 21(3–4), 71–96. <https://doi.org/10.1016/j.ocemod.2007.11.005>
- Zhang, Y., Witter, R. W., & Priest, G. P. (2011). Tsunami-tide interaction in 1964 Prince William Sound tsunami. *Ocean Modelling*, 40(3–4), 246–259. <https://doi.org/10.1016/j.ocemod.2011.09.005>
- Zhang, Y., Ye, F., Stanev, E. V., & Grashorn, S. (2016). Seamless cross-scale modeling with SCHISM. *Ocean Modelling*, 102, 64–81. <https://doi.org/10.1016/j.ocemod.2016.05.002>